



Confined Crystallization of Polyethylene Oxide in Nanolayer Assemblies

Haopeng Wang, *et al.*
Science **323**, 757 (2009);
DOI: 10.1126/science.1164601

The following resources related to this article are available online at www.sciencemag.org (this information is current as of February 6, 2009):

Updated information and services, including high-resolution figures, can be found in the online version of this article at:

<http://www.sciencemag.org/cgi/content/full/323/5915/757>

Supporting Online Material can be found at:

<http://www.sciencemag.org/cgi/content/full/323/5915/757/DC1>

This article **cites 22 articles**, 4 of which can be accessed for free:

<http://www.sciencemag.org/cgi/content/full/323/5915/757#otherarticles>

This article appears in the following **subject collections**:

Materials Science

http://www.sciencemag.org/cgi/collection/mat_sci

Information about obtaining **reprints** of this article or about obtaining **permission to reproduce this article** in whole or in part can be found at:

<http://www.sciencemag.org/about/permissions.dtl>

References and Notes

- C. Weidner, P. Kroupa, *Mon. Not. R. Astron. Soc.* **348**, 187 (2004).
- D. F. Figer, *Nature* **434**, 192 (2005).
- F. D. Kahn, *Astron. Astrophys.* **37**, 149 (1974).
- M. G. Wolfire, J. P. Cassinelli, *Astrophys. J.* **319**, 850 (1987).
- T. Nakano, T. Hasegawa, C. Norman, *Astrophys. J.* **450**, 183 (1995).
- J. Jijina, F. C. Adams, *Astrophys. J.* **462**, 874 (1996).
- H. W. Yorke, C. Sonnhalter, *Astrophys. J.* **569**, 846 (2002).
- M. M. Marinak *et al.*, *Phys. Rev. Lett.* **75**, 3677 (1995).
- F. H. Shu, S. Tremaine, F. C. Adams, S. P. Ruden, *Astrophys. J.* **358**, 495 (1990).
- M. R. Krumholz, R. I. Klein, C. F. McKee, *Astrophys. J.* **656**, 959 (2007).
- K. M. Kratter, C. D. Matzner, M. R. Krumholz, *Astrophys. J.* **681**, 375 (2008).
- B. D. Mason *et al.*, *Astron. J.* **115**, 821 (1998).
- H. Sana, E. Gosset, Y. Nazé, G. Rauw, N. Linder, *Mon. Not. R. Astron. Soc.* **386**, 447 (2008).
- C. F. McKee, J. C. Tan, *Nature* **416**, 59 (2002).
- C. F. McKee, J. C. Tan, *Astrophys. J.* **585**, 850 (2003).
- H. Beuther *et al.*, *Astron. Astrophys.* **466**, 1065 (2007).
- A. A. Goodman, P. J. Benson, G. A. Fuller, P. C. Myers, *Astrophys. J.* **406**, 528 (1993).
- R. I. Klein, *J. Comput. Appl. Math.* **109**, 123 (1999).
- M. R. Krumholz, C. F. McKee, R. I. Klein, *Astrophys. J.* **611**, 399 (2004).
- R. T. Fisher, thesis, University of California, Berkeley (2002).
- M. R. Krumholz, R. I. Klein, C. F. McKee, J. Bolstad, *Astrophys. J.* **667**, 626 (2007).
- A. I. Shestakov, S. S. R. Offner, *J. Comput. Phys.* **227**, 2154 (2008).
- See supporting material on Science Online.
- G. Lodato, W. K. M. Rice, *Mon. Not. R. Astron. Soc.* **358**, 1489 (2005).
- M. R. Bate, *Mon. Not. R. Astron. Soc.* **314**, 33 (2000).
- H. W. Yorke, P. Bodenheimer, *Astrophys. J.* **525**, 330 (1999).
- C. D. Matzner, C. F. McKee, *Astrophys. J.* **545**, 364 (2000).
- J. Alves, M. Lombardi, C. J. Lada, *Astron. Astrophys.* **462**, L17 (2007).
- M. R. Krumholz, C. F. McKee, R. I. Klein, *Astrophys. J.* **618**, L33 (2005).
- N. J. Turner, E. Quataert, H. W. Yorke, *Astrophys. J.* **662**, 1052 (2007).
- Supported by NSF grants AST-0807739 (M.R.K.) and AST-0606831 (R.I.K. and C.F.M.); the Spitzer Space Telescope Theoretical Research Program, provided by NASA through a contract issued by the Jet Propulsion Laboratory (M.R.K.); NASA through Astrophysics Theory and Fundamental Physics Program grants NAG 05-12042 and NNG 06-GH96G (R.I.K. and C.F.M.); and the U.S. Department of Energy at Lawrence Livermore National Laboratory under contract B-542762 (R.I.K., S.S.R.O., and A.J.C.). This research used the Datastar system at the NSF San Diego Supercomputer Center (grant UCB267).

Supporting Online Material

www.sciencemag.org/cgi/content/full/1165857/DC1

SOM Text

Figs. S1 to S5

Movie S1

References

12 September 2008; accepted 11 December 2008

Published online 15 January 2009;

10.1126/science.1165857

Include this information when citing this paper.

Confined Crystallization of Polyethylene Oxide in Nanolayer Assemblies

Haopeng Wang,¹ Jong K. Keum,¹ Anne Hiltner,^{1*} Eric Baer,¹ Benny Freeman,² Artur Rozanski,³ Andrzej Galeski³

The design and fabrication of ultrathin polymer layers are of increasing importance because of the rapid development of nanoscience and nanotechnology. Confined, two-dimensional crystallization of polymers presents challenges and opportunities due to the long-chain, covalently bonded nature of the macromolecule. Using an innovative layer-multiplying coextrusion process to obtain assemblies with thousands of polymer nanolayers, we discovered a morphology that emerges as confined polyethylene oxide (PEO) layers are made progressively thinner. When the thickness is confined to 20 nanometers, the PEO crystallizes as single, high-aspect-ratio lamellae that resemble single crystals. Unexpectedly, the crystallization habit imparts two orders of magnitude reduction in the gas permeability.

Crystalline polymers, such as polyethylene, polypropylene, poly(ethylene terephthalate), and nylon, have been broadly used as gas-barrier films in food, medicine, and electronics packaging, benefiting thereby from their low cost, easy processing, and mechanical toughness. Good barrier properties are imparted by the ability of polymer chains to crystallize into semi-crystalline materials with both crystalline and amorphous phases (1). The efficiency of chain packing is such that the crystalline phase is generally regarded as impermeable to even small gas molecules, and gas transport is seen as occurring through the amorphous regions (2). The processing conditions can be readily varied to control the amount of crystallinity and chain orientation and to tune the barrier properties of the final

product (3). With the growing use of polymers as thin and ultrathin films (4, 5), morphologies have been found resulting from constrained two-dimensional (2D) polymer crystallization (4, 6). These crystalline morphologies could possess gas permeability characteristics that are not expected from the bulk polymers.

Despite confinement, crystallization of polymer chains follows the conventional habit whereby polymer chains fold back and forth into stems to form crystalline lamellae with a thickness of ~10 to 20 nm. It is typical of crystallization from the isotropic melt that the lamellae are organized in a spherulitic morphology (7). However, the processes of nucleation and growth that control the crystallization kinetics can be profoundly affected by nanoscale confinement. The thickness of ultrathin polymer layers, usually a few tens of nanometers, is comparable to or a small multiple of the lamellar crystal thickness. Hence, the isotropic growth of lamellar crystals is greatly hampered, and crystallization under confinement can produce a specific lamellar crystal orientation. Often, the preferred lamellar crystal orientation is vertical to the layer (edge-on) (8, 9, 10). However, at the

other extreme, lamellar crystal orientation parallel to the layer (flat-on) is observed (6, 11–14). Although the mechanisms for the specific lamellar orientation during confined crystallization are still under investigation (15, 16), it is believed that the confined crystals will show anisotropic properties.

The 2D crystallization of polymers is conventionally studied with thin films or block copolymers that contain a crystallizable block. In the former, crystallizable layers with nanometer to submicron thicknesses are prepared by a solution process such as spin-coating (4, 17) or Langmuir-Blodgett (18) techniques. This approach is limited by the solvent requirement and by the small amount of material that can be fabricated. In the latter, a layered morphology on the nanometer scale is achieved as a consequence of microphase separation of the dissimilar blocks. If the crystallization temperature of the crystallizable block is below the order-disorder transition temperature (19), crystallization occurs with confinement in the layer-normal direction. A wide range of crystallizable blocks have been studied (8, 11–14, 16). However, elucidation of the structure-property relationships has been hindered by the need to synthesize the block copolymers and by the shear alignment that is required to construct the uniformly oriented phase structure (20).

In contrast to the self-assembled confinement created with microphase-separated block copolymers (21), layer-multiplying coextrusion uses forced assembly to create films with hundreds or thousands of alternating layers of two polymers (22, 23). Almost any melt-processable polymer can be fabricated into kilometers of nanolayered films, and layers less than 10 nm in thickness have been made. Although the amount of material in a single layer is very small, the properties of the confined layer are multiplied many-fold by the number of identical layers in the assembly. This enables us to use conventional methods to probe size-scale-dependent properties. Polyethylene oxide (PEO) was coextruded with poly

¹Department of Macromolecular Science and Engineering, Case Western Reserve University, Cleveland, OH 44106–7202, USA. ²Department of Chemical Engineering, University of Texas at Austin, Austin, TX 78758, USA. ³Centre of Molecular and Macromolecular Studies, Polish Academy of Sciences, 90–363 Lodz, Poland.

*To whom correspondence should be addressed. E-mail: ahiltner@case.edu

(ethylene-*co*-acrylic acid) (EAA), a copolymer with much lower crystallinity than PEO (fig. S1). Films with 33, 257, and 1025 alternating EAA and PEO layers were coextruded with various thicknesses and various composition ratios, including (EAA/PEO vol/vol) 50/50, 70/30, 80/20 and 90/10 (table S1). The nominal PEO layer thickness, which was calculated from the number of layers, the composition ratio, and the film thickness, varied from 3.6 μm to 8 nm. Non-layered control films were also extruded.

Permeability to small molecules is an important performance property of polymer films. Gas transport also provides a probe into the solid-state structure (3). The oxygen permeability (P) was first measured on films where the PEO and EAA layers had the same thickness. The layer thick-

ness was varied by changing the number of coextruded layers and the overall film thickness while maintaining the composition at 50/50. The results, plotted in Fig. 1A as a function of layer thickness, unexpectedly showed a steady decrease in the oxygen permeability as the EAA and PEO layers became thinner. A comparable reduction was found for carbon dioxide permeability.

The series model for layered assemblies gives the gas permeability as

$$P_{\parallel} = \left(\frac{\phi_{PEO}}{P_{PEO}} + \frac{1 - \phi_{PEO}}{P_{EAA}} \right)^{-1} \quad (1)$$

where ϕ_{PEO} is the volume fraction of PEO, and P_{PEO} and P_{EAA} are the permeabilities of PEO and EAA control films, respectively. Using the

determined values of 0.38 barrer (24) and 2.30 barrer for P_{PEO} and P_{EAA} , Eq. 1 gave the oxygen permeability of an EAA/PEO 50/50 layered assembly as 0.65 barrer. Only the film with the thickest layers conformed to this prediction.

Noting that PEO is substantially less permeable to oxygen than EAA, Eq. 1 predicts that P_{\parallel} will be quite sensitive to P_{PEO} even if ϕ_{PEO} is relatively small. To ascertain whether a dramatic change in the PEO permeability was responsible for the layer thickness effect, numerous films that varied in both the composition ratio and the layer thickness were tested. Although the measured values of P scattered, depending on the composition ratio, when an effective PEO permeability was extracted,

$$P_{PEO,eff} = \phi_{PEO} \left(\frac{1}{P} - \frac{1 - \phi_{PEO}}{P_{EAA}} \right)^{-1} \quad (2)$$

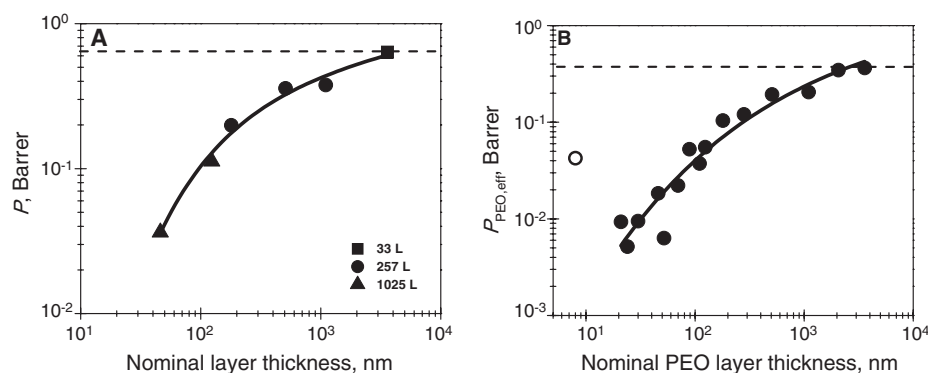


Fig. 1. The effect of layer thickness on oxygen permeability. (A) Oxygen permeability of films with equal volume fractions of EAA and PEO. The dashed line indicates P_{\parallel} calculated from Eq. 1. (B) Oxygen permeability of the PEO layers from films of varying composition calculated from Eq. 2. The dashed line indicates P_{PEO} . The open symbol is for a film with PEO layer breakup. The solid lines are drawn to guide the eyes.

the data collapsed to a single curve when $P_{PEO,eff}$ was plotted as a function of the PEO layer thickness (Fig. 1B). Only the results for the thicker PEO microlayers conformed to Eq. 2, with $P_{PEO,eff} \approx P_{PEO}$, as indicated by the dashed line. Deviation below the line was seen with 1- μm -thick PEO layers. The lowest $P_{PEO,eff}$ was achieved with 20-nm layers, and the value of 0.0052 barrer was almost 2 orders of magnitude less than P_{PEO} .

It seemed likely that crystallization in a confined space resulted in an unusual crystalline morphology that endowed the PEO nanolayers with exquisitely low permeability. However, differential scanning calorimetry revealed that even in the thinnest layers, both PEO and EAA possessed the same melting enthalpy and the same melting

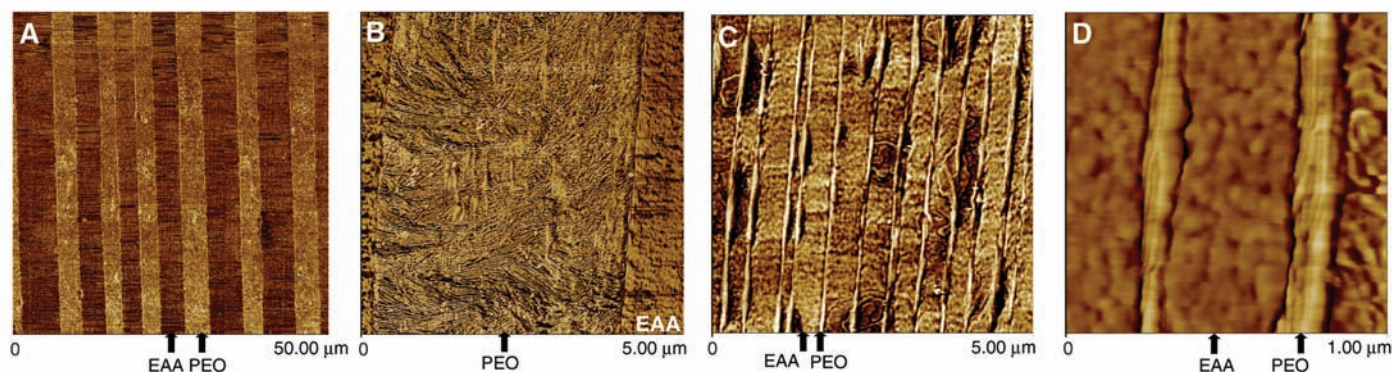
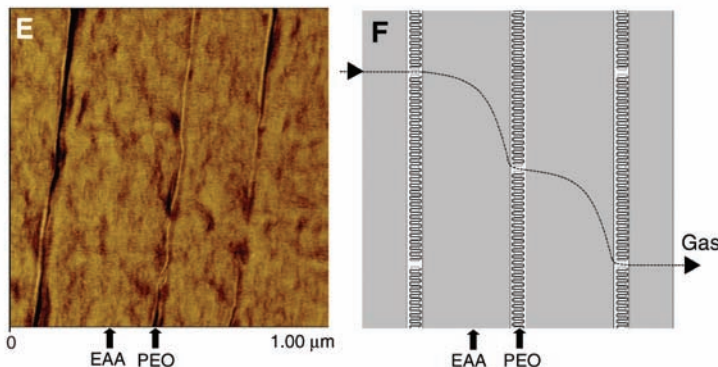


Fig. 2. AFM phase images of partial cross sections of the layered EAA/PEO films. The PEO layer has substantially higher crystallinity than the EAA layers and hence appears bright in the AFM images. (A) A low-resolution image of an EAA/PEO film with 50/50 composition, 33 alternating layers, and nominal PEO layer thickness of 3.6 μm . (B) A higher-resolution image showing the spherulitic morphology of the 3.6- μm -thick PEO layer. (C) A low-resolution image of an EAA/PEO film with 70/30 composition, 1025 alternating layers and nominal PEO layer thickness of 110 nm. (D) A higher-resolution image of the 110-nm-thick PEO layers showing the oriented stacks of PEO lamellae. (E) A high-resolution image of an EAA/PEO film with 90/10 composition, 1025 alternating layers, and nominal PEO layer thickness of 20 nm showing that the PEO layers crystallized as single, extremely large lamellae. (F) A schematic showing the gas diffusion pathway through the layered assembly with 20-nm-thick PEO layers. The arrows identify the EAA layers and PEO layers.



temperature as the control films, which were 153 J/g and 66°C for PEO, and 98 J/g and 98°C for EAA, respectively (fig. S2 and table S2). Thus, any unusual crystalline morphology that provided the very low permeability of PEO nanolayers was not accompanied by changes in the crystallinity or in the lamellar thickness.

The layers were viewed by microtoming the film through the thickness and examining the exposed surface in atomic force microscope (AFM). A region from the cross section of a film with 3.6- μm -thick PEO layers confirmed the layer continuity (Fig. 2A). Although there was some nonuniformity, the average layer thickness was close to the calculated nominal layer thickness. A higher magnification image showed the sharp boundaries between EAA and PEO layers (Fig. 2B). The spherulitic morphology of the bright PEO layer closely resembled that of PEO crystallized from the unconfined melt. It was expected that the properties of the PEO layers would also be the same and, indeed, the oxygen permeability of films with thick PEO layers closely conformed to Eq. 2 with $P_{\text{PEO,eff}} \approx P_{\text{PEO}}$.

Another pair of images in Fig. 2, C and D, compares a film with 110-nm-thick PEO layers. The images confirmed the continuity of the thin PEO layers and the close correspondence between the average layer thickness and the nominal thickness. At higher magnification, the effect of confinement on crystallization of the PEO layer shows that PEO crystallized as stacks of three to five long, thin lamellae oriented in the plane of the layer. When the PEO layer thickness was reduced to 20 nm, most of the PEO layers crystallized as single, extremely large lamellae whose lateral dimensions frequently exceeded

the field of the AFM image (Fig. 2E). Coincidence between the layer thickness, which was determined by the extrusion conditions, and the thickness of PEO lamellae, about 20 nm, facilitated crystallization of the layers as single lamellae. The single lamellae could be thought of as very large single crystals (25). If the layer thickness was reduced to 8 nm, the layers broke up, which caused the increased permeability of the film with 8-nm PEO layers.

The lamellar crystalline core is considered impermeable, and the lamellar fold surfaces constitute the permeable amorphous regions. For a single layer of flat-on lamellae, as in the PEO nanolayer, the diffusion pathway depends on the frequency of defects such as lamellar edges (Fig. 2F). Structurally, the nanolayered assembly resembles a dispersion of impermeable platelets of given aspect ratio. If the platelets are oriented perpendicular to the flux, the permeability of the composite is expressed as (26)

$$P = P_{\text{EAA}} \left[1 + \frac{\alpha^2 \phi^2}{4(1 - \phi)} \right]^{-1} \quad (3)$$

where ϕ is the volume fraction of impermeable platelets and α is the aspect ratio of the platelets defined as length divided by width. In this case, ϕ was taken as the volume fraction of the PEO crystalline phase. For the thinnest PEO nanolayers, the aspect ratio from Eq. 3 was as high as 120, which meant a lateral dimension of more than 2 μm for lamellae 20 nm thick. Gradually increasing the PEO layer thickness relaxed the restriction on 3D growth, which allowed crystallization of lamellar stacks and

permitted randomization of the lamellar orientation. Also, the increased area density of nuclei in individual layers reduced the lateral dimension of lamellae. The gradual change in crystallization habit from single lamellae to isotropic spherulites paralleled a gradual increase in the permeability of the PEO layer.

Confirmation of the oriented lamellar morphology and details of the global orientation were obtained with small-angle x-ray scattering (SAXS) and wide-angle x-ray scattering (WAXS). The SAXS examined the periodic arrangement of lamellar crystals within the constituent layers. By aligning the incident x-ray beam parallel to the normal direction (ND), the extrusion direction (ED), and the transverse direction (TD), the orientation of lamella was determined (fig. S3). The scattering patterns indicated that the long spacing of the PEO and EAA lamellae in layered films were 22.0 ± 0.6 nm and 10.8 ± 0.5 nm, respectively, nearly the same as in the control films. Isotropic scattering patterns in all three directions from 3.6 μm PEO layers indicated that the PEO layers were too thick for PEO lamellae to feel any substantial confinement effect. However, as the PEO layer thickness decreased to 110 nm, highly oriented meridional two-point scattering features appeared in the ED and TD patterns, which indicated that stacked PEO lamellae were oriented primarily parallel to the layer surface due to the confinement. The extremely weak first-order peak from 20 nm PEO layers indicated that they existed predominantly as single lamellae rather than as stacks (fig. S4).

The orientation of the PEO chains in the crystal was examined with 2D WAXS and pole

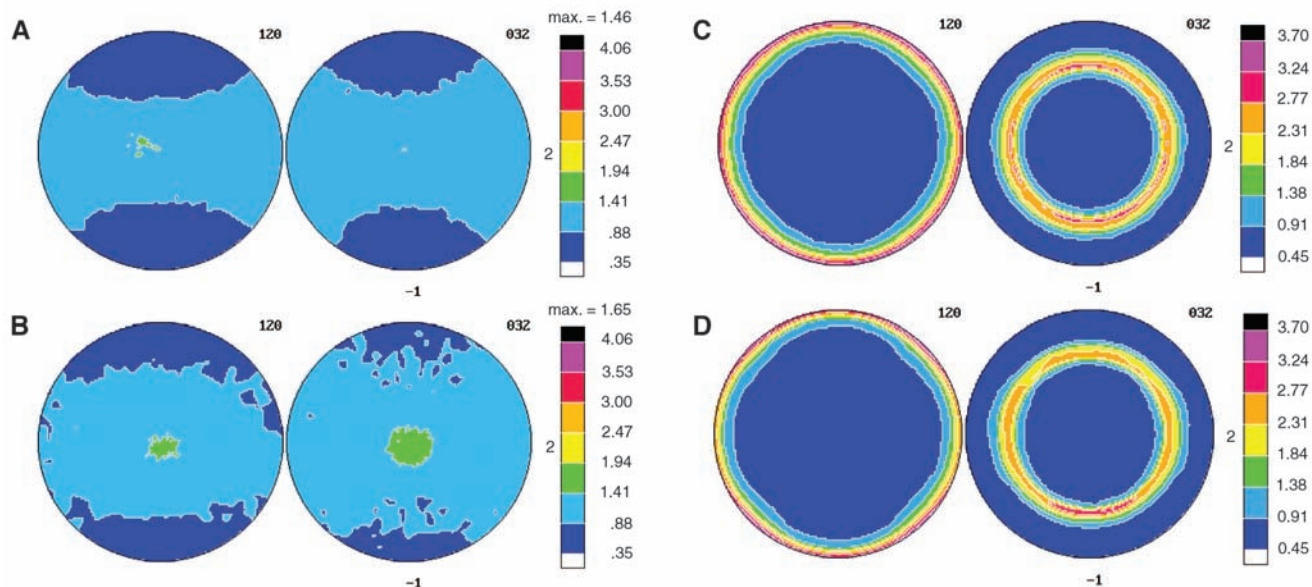


Fig. 3. Pole figures of normals to the (120) and (032) planes of the PEO monoclinic crystals (27). The extrusion direction is vertical and the transverse direction is horizontal. The normal direction is in the center of the pole figure. (A) The PEO control film. (B) An EAA/PEO film with 50/50 composition, 33 alternating layers, and nominal PEO layer thickness of 3.6 μm . (C) An EAA/PEO

film with 70/30 composition, 1025 alternating layers, and nominal PEO layer thickness of 110 nm. Orientation of the (120) planes is perpendicular to the layer plane, and orientation of the (032) planes is at 67°. (D) An EAA/PEO film with 90/10 composition, 1025 alternating layers, and nominal PEO layer thickness of 20 nm.

figures. Consistent results were obtained by these two techniques. From the pole figures of normals to the (120) and (032) planes of PEO (27), it is seen that there is no preferred orientation of crystals in the control film except for a slight orientation due to the extrusion process (Fig. 3A). In Fig. 3B, the film with 3.6- μm -thick PEO layers also showed only very weak orientation. In contrast, the film with 110-nm-thick PEO layers showed a very strong orientation of the (120) and also the (032) planes (Fig. 3C). Nearly all the (120) planes that contained polymer chains were perpendicular to the film plane. This meant that the fold surfaces of the lamellar PEO crystals were in the plane of the layer. Upon decreasing the PEO layer thickness to 20 nm, the preferred orientation of PEO lamellae parallel to the layers seemed even stronger, as indicated by the narrower ring at the pole figure circumference (Fig. 3D). The (120) planes were distributed evenly in the plane of film, always being perpendicular to the film surface. The pole figures for (032) normal in Fig. 3, C and D, resembled rings exactly offset by 67°, as predicted by the crystallographic unit cell for the preferred orientation of PEO lamellae parallel to the layer interface (16). Again, the ring for the (032) normal in Fig. 3D was much narrower than in Fig. 3C.

The crystal orientation of PEO in confined nanolayers essentially reproduced the crystal structure of PEO blocks in self-assembled PS-*b*-PEO diblock copolymers (14, 16). Comparing the sharpness of the WAXS pattern, considerably higher orientation was achieved by physically confining a high-molecular-weight PEO between

force-assembled layers than by confining a low-molecular-weight PEO block between self-assembled lamellae with covalent links. When the thickness confinement occurred on the size scale of the usual lamellar thickness, the PEO layers crystallized as single lamellae with extremely large aspect ratios. It was suggested that the lamellae could be thought of as large, impermeable single crystals.

The coextrusion process, which operates with readily available polymers, now makes it possible to fabricate nanolayered polymeric structures in sufficient quantities to probe the structure-property relationships of the morphologies resulting from nanoscale confinement. For design and execution of packaging strategies, polymer nanolayers can be incorporated into conventional polymeric films with the right barrier properties for less cost, which in turn may reduce the environmental and energy impact.

References and Notes

1. D. C. Bassett, *Principles of Polymer Morphology* (Cambridge Univ. Press, Cambridge, 1981).
2. D. H. Weinkauff, D. R. Paul, in *Barrier Polymers and Structures*, W. J. Koros, Ed. (American Chemical Society, Washington, DC 1990), pp. 60–91.
3. A. Hiltner, R. Y. F. Liu, Y. S. Hu, E. Baer, *J. Polym. Sci. Pt. B Polym. Phys.* **43**, 1047 (2005).
4. C. W. Frank *et al.*, *Science* **273**, 912 (1996).
5. S. Goffri *et al.*, *Nat. Mater.* **5**, 950 (2006).
6. G. Reiter *et al.*, *Lect. Notes Phys.* **714**, 179 (2007).
7. E. Baer, A. Hiltner, H. D. Keith, *Science* **235**, 1015 (1987).
8. I. W. Hamley *et al.*, *Macromolecules* **29**, 8835 (1996).
9. T. E. Bernal-Lara, R. Y. F. Liu, A. Hiltner, E. Baer, *Polymer (Guildf.)* **46**, 3043 (2005).
10. Y. Jin *et al.*, *J. Polym. Sci. Pt. B Polym. Phys.* **42**, 3380 (2004).
11. R. M. Ho *et al.*, *Macromolecules* **37**, 5985 (2004).
12. Y. S. Sun *et al.*, *Macromolecules* **39**, 5782 (2006).
13. U. Mukai, R. E. Cohen, A. Bellare, R. J. Albalak, *J. Appl. Polym. Sci.* **70**, 1985 (1998).
14. M.-S. Hsiao *et al.*, *Macromolecules* **41**, 8114 (2008).
15. Y. Ma, W. Hu, G. Reiter, *Macromolecules* **39**, 5159 (2006).
16. L. Zhu *et al.*, *J. Am. Chem. Soc.* **122**, 5957 (2000).
17. S. Napolitano, M. Wübbenhorst, *J. Phys. Condens. Matter* **19**, 205121 (2007).
18. B. Li, A. R. Esker, *Langmuir* **23**, 2546 (2007).
19. F. S. Bates, G. H. Fredrickson, *Annu. Rev. Phys. Chem.* **41**, 525 (1990).
20. Z.-R. Chen, J. A. Kornfield, S. D. Smith, J. T. Grothaus, M. M. Sattkowski, *Science* **277**, 1248 (1997).
21. G. M. Whitesides, B. Grzybowski, *Science* **295**, 2418 (2002).
22. R. Y. F. Liu, Y. Jin, A. Hiltner, E. Baer, *Macromol. Rapid Commun.* **24**, 943 (2003).
23. R. Y. F. Liu, T. E. Bernal-Lara, A. Hiltner, E. Baer, *Macromolecules* **37**, 6972 (2004).
24. 1 Barrer = $10^{10} \frac{\text{cm}^3(\text{STP})\text{cm}}{\text{cm}^2 \text{ s cmHg}}$ where STP is standard temperature and pressure.
25. P. H. Geil, *Polymer Single Crystals* (Wiley-Interscience, New York, 1963).
26. E. L. Cussler, S. E. Hughes, W. J. Ward III, R. Aris, *J. Membr. Sci.* **38**, 161 (1988).
27. The PEO reflection labeled (032) actually contains overlapped reflections from (032), ($\bar{1}$ 32), (112), ($\bar{2}$ 12), ($\bar{1}$ 24), ($\bar{2}$ 04), and (004), which have similar *d*-spacing of ~0.39 nm, with that from (032) being the strongest. They cannot be easily separated in (032) pole figure. Details can be found in (16).
28. This research was supported by the NSF Center for Layered Polymeric Systems (grant DMR-0423914).

Supporting Online Material

www.sciencemag.org/cgi/content/full/323/5915/757/DC1
Materials and Methods

SOM Text

Figs. S1 to S5

Tables S1 and S2

References

13 August 2008; accepted 26 November 2008
10.1126/science.1164601

Nitrogen-Doped Carbon Nanotube Arrays with High Electrocatalytic Activity for Oxygen Reduction

Kuanping Gong,¹ Feng Du,¹ Zhenhai Xia,² Michael Durstock,³ Liming Dai^{1,4*}

The large-scale practical application of fuel cells will be difficult to realize if the expensive platinum-based electrocatalysts for oxygen reduction reactions (ORRs) cannot be replaced by other efficient, low-cost, and stable electrodes. Here, we report that vertically aligned nitrogen-containing carbon nanotubes (VA-NCNTs) can act as a metal-free electrode with a much better electrocatalytic activity, long-term operation stability, and tolerance to crossover effect than platinum for oxygen reduction in alkaline fuel cells. In air-saturated 0.1 molar potassium hydroxide, we observed a steady-state output potential of –80 millivolts and a current density of 4.1 milliamps per square centimeter at –0.22 volts, compared with –85 millivolts and 1.1 milliamps per square centimeter at –0.20 volts for a platinum-carbon electrode. The incorporation of electron-accepting nitrogen atoms in the conjugated nanotube carbon plane appears to impart a relatively high positive charge density on adjacent carbon atoms. This effect, coupled with aligning the NCNTs, provides a four-electron pathway for the ORR on VA-NCNTs with a superb performance.

The oxygen reduction reaction (ORR) at the cathode of fuel cells (1) plays a key role in controlling the performance of a fuel cell, and efficient ORR electrocatalysts are essential for practical applications of the fuel cells (2, 3).

The ORR can proceed either through (i) a four-electron process to combine oxygen with electrons and protons directly, when coupled with oxidation on the anode, to produce water as the end product, or (ii) a less efficient two-step, two-electron path-

way involving the formation of hydrogen peroxide ions as an intermediate (2, 3). Alkaline fuel cells with platinum-loaded carbon as an electrocatalyst for the four-electron ORR were developed for the Apollo lunar mission in the 1960s (4), but their large-scale commercial application has been precluded by the high cost of the requisite noble metals. Apart from its high cost, the Pt-based electrode also suffers from its susceptibility to time-dependent drift (5) and CO deactivation (6).

Recent intensive research efforts in reducing or replacing Pt-based electrode in fuel cells have led to the development of new ORR electrocatalysts, including Pt-based alloys (7), transition metal chalcogenides (8), carbon nanotube-supported metal particles (9–11), enzymatic electrocatalytic systems (12), and even conducting poly(3,4-

¹Departments of Chemical and Materials Engineering, University of Dayton, 300 College Park, Dayton, OH 45469, USA.

²Department of Mechanical Engineering, University of Akron, Akron, OH 44325, USA. ³Materials and Manufacturing Directorate, Air Force Research Laboratory, RXBP, Wright-Patterson Air Force Base, OH 45433, USA. ⁴Department of Chemistry and University of Dayton Research Institute and Institute for the Development and Commercialization of Advanced Sensor Technology and Wright Brothers Institute, Dayton, OH 45469, USA.

*To whom correspondence should be addressed. E-mail: ldai@udayton.edu